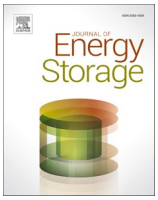
Journal of Energy Storage 180 (2026) 124353



Contents lists available at ScienceDirect

Journal of Energy Storage

journal homepage: www.elsevier.com/locate/est



Research papers



State-of-health estimation of lithium-ion batteries subjected to different ageing conditions via electrochemical impedance spectroscopy and machine learning

Emmanuel Ezeoba [a,b,c,*], Sehriban Celik [a,b,c], Gereon Stahl [a,b,c], Dirk Uwe Sauer [a,b,c,d]

[a] Chair for Electrochemical Energy Conversion and Storage Systems, Institute for Power Electronics and Electrical Drives (ISEA), RWTH Aachen University, Campus-Boulevard 89, Aachen, 52074, Germany
[b] Center for Ageing, Reliability and Lifetime Prediction of Electrochemical and Power Electronic Systems (CARL), RWTH Aachen University, Campus-Boulevard 89, Aachen, 52074, Germany
[c] Jülich Aachen Research Alliance, JARA-Energy, Jülich, 52425, Germany
[d] Helmholtz Institute Münster (HIMS), IMD-4, Forschungszentrum Jülich, Jülich, 52425, Germany

ARTICLE INFO

Keywords:
Lithium-ion battery
Electrochemical impedance spectroscopy
Equivalent circuit model
Machine learning
Ensemble model
State-of-health

ABSTRACT

State-of-health estimation is essential for the safe and reliable operation of lithium-ion batteries, particularly under diverse real-world operating conditions. This study presents a hybrid framework that combines electrochemical impedance spectroscopy with machine learning for battery State-of-health estimation. Electrochemical impedance spectroscopy measurements were acquired from full lithium-ion cells aged under fourteen distinct operating conditions, providing a broad range of degradation trajectories for model development and evaluation. Two compact feature representations were compared: parameters obtained from equivalent circuit model fitting and band-compressed statistical descriptors calculated directly from the impedance spectra. These feature sets were used independently to train a stacking ensemble comprising XGBoost and Random Forest regressors with a linear regression meta-learner. Both feature representations achieved comparable state-of-health prediction performance, with root-mean-square errors below 3%. Feature-importance analysis showed that only a small subset of features contributed most of the predictive capability. The results show that compact electrochemical impedance spectroscopy feature representations can provide reliable and computationally efficient inputs for data-driven state-of-health estimation, offering a practical complementary approach for impedance-based battery diagnostics.

1. Introduction

The state-of-health (SoH) of lithium-ion batteries can be obtained directly by fully charging and then completely discharging the battery at a constant current rate. The SoH is determined by comparing the discharged capacity of the battery to its original or nominal capacity [1,2]. Alternatively, the SoH can also be expressed in terms of the measured internal resistance as a percentage of its initial value [2] at the beginning of battery life. Although these approaches to SoH estimation are suitable in a controlled laboratory environment, they are often impractical for real-world applications because they require interruption of normal operation, long testing times, and are sensitive to operating conditions and environmental factors [3]. Accurate SoH estimation remains an important aspect of improving safety, optimizing operational strategies, and reducing user anxiety in adopting lithium-ion batteries for applications such as electric vehicles [4]. Existing methods frequently rely on extensive charge-discharge testing or laboratory-based measurements, limiting their suitability for online battery management [5]. Coulomb counting estimates SoH indirectly by tracking the accumulated ampere-hour (Ah) throughput during charge and discharge cycles; consequently, its accuracy depends heavily on precise current integration and reliable monitoring by the battery management system [6]. These limitations motivate the development of complementary diagnostic approaches that can provide efficient SoH estimation with reduced dependence on strict

* Corresponding author at: RWTH Aachen University, Campus-Boulevard 89, 52074, Aachen, Germany.
E-mail addresses: emmanuel.ezeoba@isea.rwth-aachen.de (E. Ezeoba), sehriban.celik@isea.rwth-aachen.de (S. Celik), gereon.stahl@isea.rwth-aachen.de (G. Stahl), dirkuwe.sauer@isea.rwth-aachen.de (D.U. Sauer).

https://doi.org/10.1016/j.est.2026.124353
Received 28 May 2026; Received in revised form 11 August 2026; Accepted 19 August 2026
Available online 21 August 2026
2352-152X/© 2026 The Author(s). Published by Elsevier Ltd. This is an open access article under the CC BY license (http://creativecommons.org/licenses/by/4.0/).

operational constraints.

Electrochemical impedance spectroscopy (EIS) is a strong diagnostic tool for electrochemical systems. It provides information about underlying electrochemical processes through relatively fast and non-destructive measurements. By applying small perturbations across a wide frequency spectrum and exploiting the frequency-dependent response of the system, EIS offers insights into the internal state of the battery [7]. However, despite its rich information about battery state, the high dimensionality and redundancy of impedance spectra present challenges for machine learning (ML) models. Adjacent frequency points often contain highly correlated information, increasing computational complexity and the risk of overfitting without necessarily improving predictive performance. It therefore remains unclear whether the ageing information contained in the full impedance spectrum can be represented more compactly while preserving information relevant for SoH prediction, and which compact representation is most effective for this purpose. This motivates the development of compact feature representations that retain the electrochemical information most relevant to battery degradation while reducing redundancy in the input data. Consequently, ML methods have increasingly been explored to exploit these diagnostic features for battery SoH estimation. Zhang et al. applied Gaussian process regression (GPR) directly to raw impedance spectra [8], while Fu et al. employed an extreme learning machine (ELM), a single-hidden-layer neural network, using frequency-domain features with regularization, with both approaches achieving capacity estimation errors below 2% [9]. Lu et al. developed a domain-adaptive deep learning framework for SoH estimation across different battery chemistries. The method achieved an absolute error below 3% without requiring labeled degradation data from the target system [10]. These approaches demonstrate the ability of ML models to capture complex relationships between ageing features and battery health.

In this study, we propose an ensemble learning approach for lithium-ion battery SoH estimation that combines Random Forest and XGBoost regressors. Two compact feature representations derived from EIS measurements are investigated: a physics-informed representation based on equivalent circuit model (ECM) parameters and a data-driven representation based on statistical descriptors extracted from selected impedance frequency bands. For each representation, a separate stacking ensemble was trained using the same Input features, enabling a direct comparison of the predictive capability and feature importance of the two approaches. Although studies have demonstrated good SoH estimation using raw EIS spectra, these approaches typically rely on a large number of highly correlated impedance values [8]. Such high-dimensional inputs increase computational complexity and may introduce redundant information without necessarily improving predictive performance. This work therefore investigates whether comparable SoH estimation accuracy can be achieved with compact feature representations that retain the most relevant electrochemical information while substantially reducing the dimensionality of the input data. Although EIS-based ML has demonstrated promising results, many existing studies are based on relatively limited datasets comprising a small number of cells or only a few ageing conditions. Such datasets provide limited diversity in degradation trajectories, making it difficult to assess model robustness across different ageing behaviors. The dataset used in this work is distinguished by measurements from full lithium-ion cells aged under fourteen conditions, enabling a more comprehensive assessment of the trade-off between physical interpretability, feature compactness, and predictive performance.

1.1. Electrochemical impedance modeling

EIS is a non-invasive, non-destructive, and relatively fast technique that measures the impedance of an electrochemical system across a range of frequencies [11]. It relies on applying a small alternating current or voltage perturbation to the system, and the response (voltage or current) is measured and analyzed [7,12]. The impedance behavior is characterized as a function of perturbing frequency, with different electrochemical processes dominating distinct frequency regions. At high frequencies, the response is primarily dominated by inductive effects and ohmic resistances arising from the electrolyte, current collectors, and contacts [13]. In the mid-frequency range, interfacial processes such as charge-transfer reactions and double-layer capacitance become dominant [13]. At low frequencies, the impedance response is dominated by mass-transport limitations arising from lithium-ion diffusion within the electrodes [13,14].

In ECM modeling, the complex electrochemical processes within a lithium-ion battery are approximated by combining electrical components such as resistors, capacitors, and inductors [15,16]. This enables easier analysis and simulation while maintaining a physical interpretation of processes within the cell [17]. Because electrochemical processes occur over different characteristic time scales, they contribute to different regions of the impedance spectrum [18]. In ECM-based impedance modeling, these responses are represented by electrical circuit elements whose characteristic time constants approximate the dominant electrochemical behavior. In practice, these time constants often represent compressed, single-valued approximations of broader underlying process distributions. Consequently, multiple ECM configurations can often provide acceptable fits to the same impedance spectrum, making model selection a trade-off between fitting accuracy, model complexity, and physical interpretability. For this reason, ECMs aim to reproduce the measured impedance response accurately using as few parameters as possible, with circuit topology chosen to balance fitting accuracy and minimal redundancy. For most practical purposes, ECMs are fitted to the Nyquist plot because it directly relates impedance features to equivalent circuit elements and provides a relatively straightforward basis for parameter estimation. Within an ECM, resistors describe ohmic and charge-transfer processes, while capacitors represent ideal capacitive behavior. Together, they define characteristic time constants $\tau = R \times C$ that approximate the characteristic response times of the underlying electrochemical processes [12]. When modeling actual experimental data, the capacitive effect is sometimes modeled using a constant phase element (CPE) to account for non-ideal behavior arising from electrode surface roughness, inhomogeneities, and other imperfections within the cell.

1.2. Machine learning in SoH estimation

Data-driven ML methods have become increasingly prominent for battery SoH estimation due to their ability to capture complex, nonlinear relationships between operating conditions and degradation trends [19]. Unlike physics-based models, which require detailed material parameters and are often computationally expensive [20,21], data-driven models can be more readily adapted to different operating conditions and battery datasets without requiring explicit electrochemical parameterization. This reframes SoH estimation as a ML regression task, rather than a purely physics-based estimation problem [22]. Among traditional ML approaches, Support Vector Regression (SVR) has been widely used for its strong generalization capability, particularly on small- to medium-sized datasets [23]. However, its predictive performance is sensitive to the kernel and hyperparameter selection, and its computational cost increases rapidly with dataset size [24]. Deep learning models, such as Convolutional Neural Networks (CNNs) and Long Short-Term Memory (LSTM) networks, have also been explored for SoH estimation [25,26]. CNNs are particularly effective at identifying local correlations and characteristic patterns within structured inputs such as voltage curves and impedance spectra [27], while LSTM networks capture temporal dependencies in sequential degradation data [28]. This makes them well-suited for modeling degradation over multiple charge-discharge cycles. Despite their strengths, these models typically require large datasets and substantial computational resources [29].

To improve generalization under limited training data or varying

Table 1
Shows the cell technical specifications as provided by the manufacturer.

Cell specification	Value
Cell chemistry	NMC622|Graphite
Capacity (Ah)	1
Cathode/Anode areal capacity (mAh/cm2)	2.24/2.7
Voltage limits (V)	3.0–4.2
Cathode/Anode porosity (%)	31.30/31.80
Cathode/Anode thickness double-sided without foil (μm)	85/100
Max charge/discharge current (C)	1.5/3
Cell dimension (mm x mm)	51 × 66
Cell stack type	Stacked

operating conditions, transfer learning and hybrid ML frameworks have also been investigated [30,31]. Gaussian process–XGBoost models combine probabilistic uncertainty estimation with boosted tree ensembles and have demonstrated improved prediction accuracy over individual models [32,33]. Among data-driven approaches, tree-based ensemble methods have become particularly attractive for battery SoH estimation due to their suitability for tabular datasets and their ability to capture complex nonlinear relationships between degradation features and battery health. Tree-based ensemble methods are well suited to this type of structured tabular data because they require minimal feature engineering, naturally capture nonlinear feature interactions, and are comparatively robust to multicollinearity and varying feature scales [34,35]. In addition, these models provide feature-importance rankings, enabling analysis of the relative contribution of different input features to SoH prediction. Random Forest and XGBoost exhibit complementary learning characteristics. Random Forest reduces prediction variance through bootstrap aggregation [36], while XGBoost sequentially minimizes residual errors to improve predictive accuracy [37]. Combining both models within a stacking framework therefore enables the meta-learner to exploit the strengths of each individual algorithm while improving overall robustness and generalization.

2. Measurement method

This section outlines the methodology used in our study. We begin with the preparation and formation of the cells, followed by the development of a test matrix detailing the cycling conditions and the acquisition of EIS measurements at different SoH levels. The proposed ML model is then introduced. Finally, the predictive performance of the model using EIS-derived features as input is compared with that of the model using ECM parameters to evaluate the relative performance of the model on each dataset.

2.1. Cell formation and ageing

Lithium-ion batteries with a nominal capacity of 1 Ah were purchased from LiFUN Technologies without electrolyte. Technical specifications of the cell as provided by the supplier are summarized in Table 1 After drying under vacuum at 80 °C for 24 h, the cells were filled with 2.8 ml of electrolyte (1 M $LiPF_6$ EC/EMC 3:7, 2 wt% VC) in a dry room with dew point of −55 ppm and allowed to wet for 12 h while held at 1.5 V. Formation cycles was carried out at 25 °C, consisting of an initial C/20 charge and C/10 discharge within a voltage window of 3.0–4.2 V, followed by two additional C/10 charge-discharge cycles. After the formation cycles, the cells were degassed and resealed using a vacuum sealer. In total, 42 cells were prepared and cycled under fourteen different conditions, with three cells per condition to show reproducibility of the results. After formation, the cells were clamped between two pressure plates to emulate the mechanical constraints experienced within a battery pack. Springs were incorporated into the setup to accommodate limited expansion in the event of excessive buildup of internal pressure. EIS measurements were acquired at defined intervals during cycling to monitor the evolution of the cells as they age. Each cell was cycled up to 2150 full cycles under a single test condition, as specified in Table 2.

Table 2
Shows the different conditions under which the cells were cycled.

Test ID	Temperature[°C]	Charge-rate	Discharge-rate	Rest time [h]
TM1	25	0.5	0.5	2
TM2	45	0.5	1.5	2
TM3	45	0.5	0.5	0
TM4	45	1.5	1.5	2
TM5	25	0.5	0.5	0
TM6	25	1.5	1.5	0
TM7	25	1.5	0.5	2
TM8	25	0.5	1.5	2
TM9	45	1.5	1.5	0
TM10	45	0.5	0.5	2
TM11	25	0.5	1.5	0
TM12	45	0.5	1.5	0
TM13	45	1.5	0.5	2
TM14	45	1.5	0.5	0

2.2. EIS measurement

During testing, over 900 EIS measurements were obtained. All measurements were performed at 25 °C in a 53 l Binder climate chamber, with the cell state of charge (SoC) set to 50% of the remaining capacity. Potentiostatic EIS measurements were performed using the Zahner Zennium EIS device at 74 frequency points over a range of 10 mHz to 50 kHz using a perturbation voltage signal of amplitude 10 mV in multisine mode. The rest time between testing and EIS measurement varied from the intended 12 h to two days. While this may introduce some variability, the spectra were measured after a relaxation period intended to reduce transient effects [38]. An ECM model was used to fit the EIS data, allowing for the extraction of model parameters using the *ImpedancePy* tool [39].

2.3. State estimation model and data preprocessing

The proposed ML framework employs a stacking ensemble architecture consisting of XGBoost and Random Forest regressors as base learners. Each base learner is independently trained using the same input feature representation, with the SoH as the dependent variable. Rather than directly combining their in-sample predictions, the stacking procedure follows a two-level learning strategy. During training, the base learners are evaluated using five-fold grouped cross-validation (GroupKFold), with grouping performed at the cell level to ensure that all EIS measurements from a given cell remain within the same fold. For each fold, the base learners are trained on four folds and used to predict the held-out fold, thereby generating out-of-fold predictions for every training sample. These out-of-fold predictions are subsequently used to train a linear regression meta-learner, which learns how to combine the predictions from both base models. After training the meta-learner, the XGBoost and Random Forest models are retrained using the complete training dataset. During inference, predictions from these retrained base learners are passed to the meta-learner to generate the final SoH estimate for previously unseen cells. By training the meta-learner exclusively on out-of-fold predictions, the proposed stacking framework reduces the risk of information leakage and overfitting associated with conventional in-sample stacking.

The XGBoost model was configured with a moderate learning rate and a relatively large number of estimators, allowing the model to learn complex patterns progressively while maintaining generalization through regularization and subsampling. Tree depth and subsampling were selected to provide sufficient model flexibility. The Random Forest regressor was configured with a moderate number of trees of limited depth, allowing it to capture nonlinear relationships while maintaining model simplicity. The hyperparameter values used for each model are

Table 3
Shows the model hyperparameter settings for ensemble learning.

XGBoost Hyperparameter	Value
n_estimator	500
learning_rate	0.05
max_depth	5
min_child_weight	1
subsample	0.5
colsample_bytree	1
objective	'reg:squarederror'
random_state	42

Random Forest Regressor Hyperparameter	Value
n_estimator	100
max_depth	10
criterion	'squared_error'
random_state	42

summarized in Table 3.

Before model training, a preprocessing step was applied to remove measurement artefacts originating from variations in the experimental setup rather than from battery degradation. During periodic reference performance tests, cells were repeatedly transferred between devices. This handling occasionally introduced small variations in electrical contact resistance, which manifest primarily as shifts in the high-frequency intercept of the impedance spectrum. For the raw EIS data, the impedance measured at 6.7 kHz, corresponding to the high-frequency intercept of the Nyquist plot, was used as the quality-control indicator. For the ECM-based representation, the fitted parameter R0, which models this same high-frequency intercept, was used. These quantities were used as quality-control indicators for identifying measurements affected by the contact resistance. Measurements with R0 or |Z| at 6.7 kHz lying outside the interval defined by the 10th and 90th percentiles were excluded. This procedure was intended to remove only obvious measurement artefacts while preserving the full range of battery ageing states.

After preprocessing, the EIS data were transformed from their real and imaginary components into impedance magnitude (|Z|) to reduce redundancy while preserving electrochemical information. To mitigate overfitting and reduce computational complexity from high-dimensional spectra, we segmented the impedance data into low- (10 mHz–1 Hz), mid- (1 Hz–1 kHz), and high- (1 kHz–50 kHz) frequency bands. Within each frequency band, statistical descriptors—mean |Z|, log-log slope |Z| vs frequency (log-log |Z|), and interquartile range |Z|—are derived. The frequency bands are selected from windows where the log-log |Z| plot shows approximately linear behavior from the EIS measurement at the beginning-of-life. This band-based feature engineering approach achieves substantial dimensionality reduction while preserving electrochemical signatures relevant to degradation processes. Although cell ageing causes characteristic frequencies to shift over time, fixed-frequency bands were used here as a consistent, model-independent way to summarize spectral evolution. The extracted features, therefore, do not assume a one-to-one mapping between frequency bands and specific electrochemical processes, but instead capture ageing-induced changes in impedance shape within the spectral regions.

Additionally, collinearity pruning is applied to all features across both data sets to further eliminate redundancy in the input features. For each pair of features with a Pearson correlation coefficient greater than 0.9, one feature was removed. By retaining only weakly correlated features, the model benefits from improved numerical stability. Following feature extraction and correlation pruning, the dataset was partitioned into training and testing sets. Cell-wise GroupShuffleSplit was used to ensure that all features from a given cell were assigned exclusively to either the training or test set, thereby preventing information leakage arising from highly correlated measurements belonging to the same degradation trajectory. The training set was subsequently divided into training and validation subsets using a second GroupShuffleSplit, again preserving cell-wise separation. Feature normalization was performed using Min–Max scaling, with scaling parameters determined from the training data and subsequently applied unchanged to the validation and test sets. To compensate for the relatively limited number of measurements at low SoH, training samples with SoH below 80% were assigned a weight of 1.5 during optimization of both base learners, while all remaining samples were assigned a weight of 1.0.

2.4. Performance evaluation metrics

The performance of the proposed model is quantitatively evaluated using three widely adopted regression metrics: root-mean-square error (RMSE), mean absolute error (MAE), and the coefficient of determination (R^2). These metrics provide complementary perspectives on the prediction accuracy and overall estimation performance of the model. The RMSE measures the square root of the average of the squared differences between the predicted SoH values and the corresponding SoH measurement. It is defined as:

$$RMSE = \sqrt{\frac{1}{N}\sum_{i=1}^{N}(\hat{y}_i - y_i)^2} \tag{1}$$

Where y_i and $\hat{y}_i$ denote the measured and predicted SoH values, respectively, and N is the number of samples. RMSE penalizes larger estimation errors more heavily due to the squaring of residuals and is therefore sensitive to large deviations between predicted and measured SoH. The MAE computes the average of the absolute differences between predicted and actual SoH values and is given by:

$$MAE = \frac{1}{N}\sum_{i=1}^{N}|\hat{y}_i - y_i| \tag{2}$$

Compared to RMSE, MAE provides a more direct interpretation of the average estimation error and is less influenced by large deviations, providing an intuitive measure of the typical prediction error. In our case, low RMSE and MAE values indicate good model estimation performance. The coefficient of determination, R^2, quantifies how much of the variability in the measured SoH can be accounted for by the input Features of the model, showing the degree to which the predicted values follow the overall degradation trend, and is expressed as:

$$R^2 = 1 - \frac{\sum_{i=1}^{N}(\hat{y}_i - y_i)^2}{\sum_{i=1}^{N}(y_i - \bar{y})^2} \tag{3}$$

Where $\bar{y}$ represents the mean of the measured SoH values. An R^2 value close to 1 indicates strong agreement between predicted and measured SoH, while lower values suggest reduced explanatory power. In combination, RMSE and MAE quantify the absolute accuracy of the SoH predictions, while R^2 evaluates how well the model follows the measured SoH evolution over the ageing process.

3. Results and discussion

This section presents the results of the proposed SoH estimation framework. First, an overview of cell degradation under the different cycling conditions is presented. The ECM used to fit the EIS data and the corresponding fitting quality are then discussed. This is followed by the preprocessing and extraction of the input features. Next, feature-importance analysis is performed to identify the most influential impedance characteristics and ECM parameters contributing to SoH prediction. Finally, the predictive performance of the model is evaluated using both ECM-based parameters and band-compressed EIS-derived

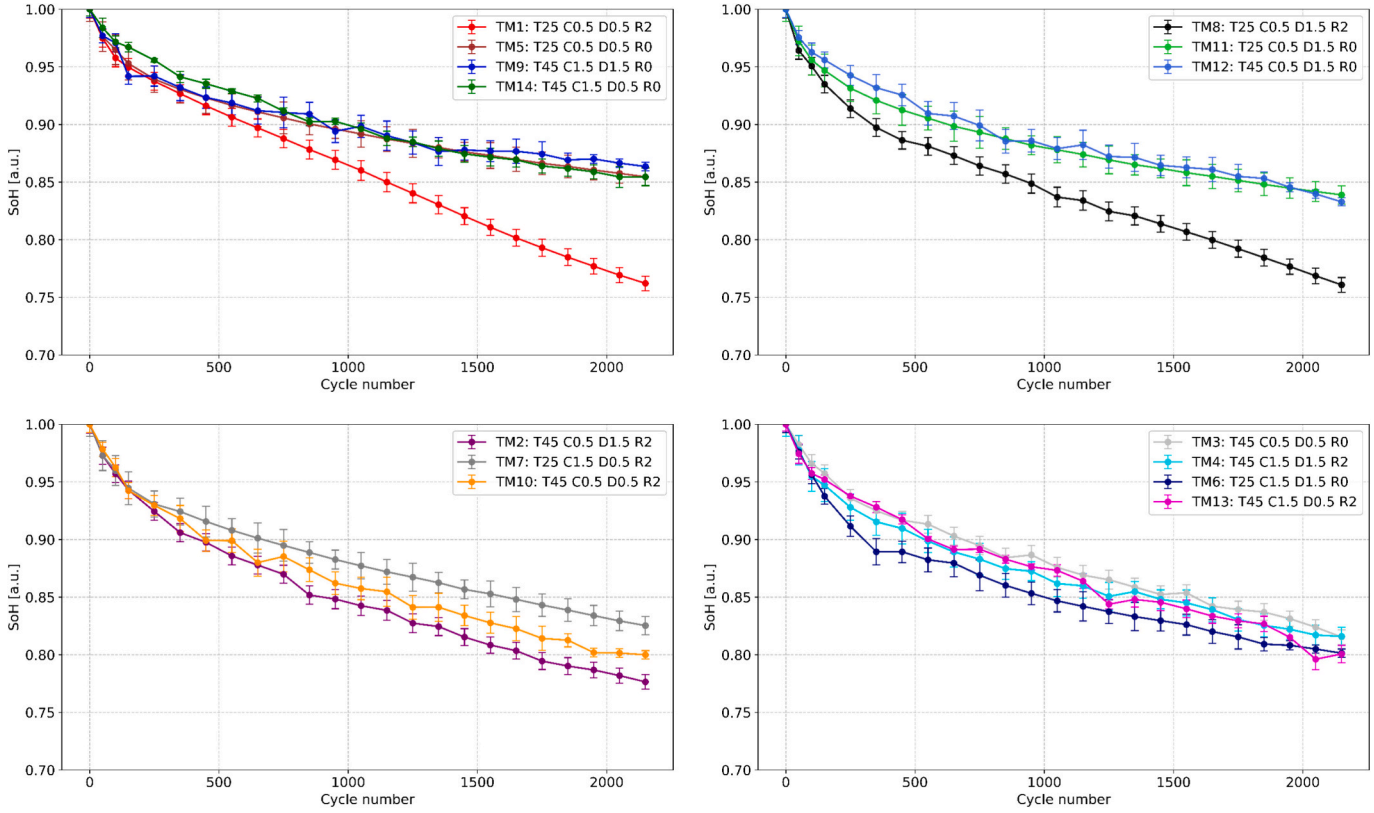


Fig. 1. Shows the average state-of-health of the cells at different test conditions. The standard deviation between the cells is shown as the error bars. The legend summarizes the cycling temperature(T), the charge and discharge current rates (C and D), and the duration of the rest time (R). The plots are shown separately to improve visual clarity.

features, including comparisons between the full and reduced feature sets.

3.1. State-of-health evolution

The SoH of three replicate cells was monitored for each test condition to quantify the progression of cell ageing under different test conditions. Fig. 1 presents the mean SoH of replicate cells of each test condition as a function of cycle number. For clarity, the data are presented across four separate plots. The error bars represent the standard deviation from the mean, reflecting the SoH variation among the replicate cells. Across all test conditions, the maximum variation in capacity among replicate cells

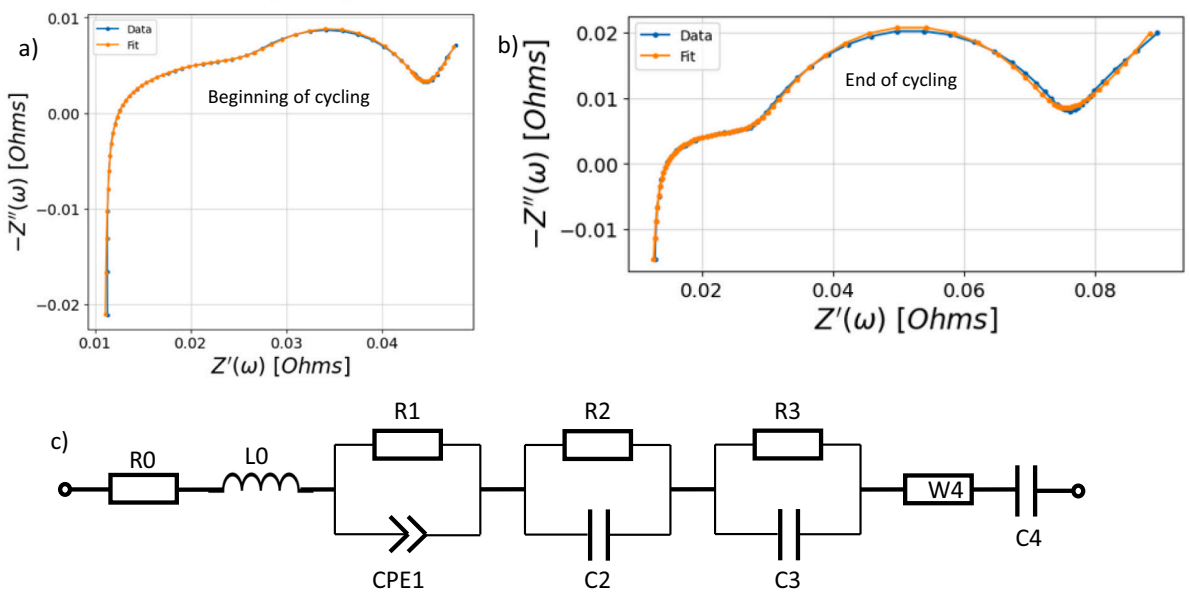


Fig. 2. Nyquist plots showing experimental impedance data (blue) and fitted models (orange) (a) at the beginning of cycling and (b) at the end of cycling. (c) An equivalent circuit model is used to fit the measured EIS data.

Table 4
Overview of the input features used in the machine learning model, comprising fitted ECM parameters and statistical descriptors extracted from band-compressed EIS spectra.

ECM parameters	EIS-derived features
L0	Low frequency |Z| mean
R0	Mid frequency |Z| mean
R1	High frequency |Z| mean
CPE1	Low frequency log-log |Z| slope
R2	Mid frequency log-log |Z| slope
C2	High frequency log-log |Z| slope
R3	Low frequency |Z| IQR
C3	Mid frequency |Z| IQR
W4	High frequency |Z| IQR
C4	—

is less than 2% of nominal cell capacity, indicating uniformity in cell behavior within the test conditions. At the end of testing, most cells retained capacities of about 80% SoH, with condition-dependent trends in degradation behavior observed depending on the ageing metrics considered.

Lower temperature cycling at 25 °C induced a faster decline in SoH with respect to cycle number than 45 °C cycling, while extended rest periods between charge and discharge also accelerated the SoH decline compared to continuous cycling. The results indicate that lower operating temperature and intermittent resting can exacerbate degradation processes through slower charge carrier mobility and parasitic side reactions at high SoCs, respectively. On the other hand, certain test conditions showed identical ageing trends. This similarity indicates that, despite differences in the imposed cycling conditions, the cells experienced comparable cumulative degradation, although the ageing modes might still differ. Further details on the ageing behavior and mechanistic interpretation of these cells are presented in [40].

3.2. Equivalent circuit model

Based on the characteristic features of the measured EIS spectra, an ECM topology comprising one R-CPE branch and two RC branches, along with an inductor, resistor, Warburg element, and capacitor connected in series, was adopted, as shown in Fig. 2c. Representative fits demonstrating the quality of the model on EIS data at the beginning and end of cycling are shown in Fig. 2a and b. The selected ECM provides a consistent fit to the EIS data across the entire test conditions, achieving a maximum RMSE on the order of 10^{-4} Ω. Simpler ECM topologies with fewer elements resulted in fit errors approximately two orders of magnitude higher, while adding further elements to the selected topology did not provide a meaningful improvement in the fitting error. This comparison supports the selection of the present topology as a balance between fitting accuracy and model complexity. The series-connected inductor L0 accounts for the inductive behavior of the connecting cables at high frequencies, while the resistor R0 models the bulk resistance of the cell materials and current collectors. The parallel combination of R1-CPE1 is used to model the solid electrolyte interphase (SEI) layer, while the R2-C2 and R3-C3 branches represent charge-transfer processes at the anode and cathode, respectively [41]. It should be noted that the selected ECM is not unique and that alternative circuit topologies may provide similarly accurate representations of the measured spectra. The model adopted here was selected as a compromise between fitting accuracy, physical interpretability, and model complexity, providing a compact and consistent set of features for subsequent ML analysis.

The input features derived from both representations are summarized in Table 4. The table lists the parameters obtained from the ECM, along with the statistical descriptors extracted from the band-compressed EIS data. The correlation matrices for the EIS-derived features and ECM parameters are presented in Figs. 1 and 2 of the supplementary information, respectively. Some correlation between the CPE parameters is expected, since both jointly describe the same distributed impedance response. For the EIS-derived representation, relatively higher correlations are primarily confined to features within the same frequency band. The high-frequency band log-log |Z| slope was pruned out due to its high correlation with high-frequency |Z| IQR.

3.3. Feature importance analysis

Applying the quality-control filtering procedure resulted in the exclusion of only four impedance measurements from the complete dataset. These excluded measurements were identified as measurement artefacts not representative of the cell ageing behavior. Therefore, the filtering step had a negligible impact on the overall SoH and ageing-condition distribution of the dataset. Feature importance analysis was performed to identify which ECM parameters and band-compressed EIS features contribute most strongly to SoH estimation after collinearity pruning. Fig. 3a and b summarize the relative importance of the remaining features as determined by the XGBoost base learner used in the ensemble. Feature importance analysis was performed to identify which ECM parameters and band-compressed EIS features contribute most strongly to SoH estimation after collinearity pruning. Fig. 3a and b summarize the relative importance of the remaining features as determined by the XGBoost base learner used in the ensemble. For the EIS-derived feature set, the most influential features are associated with the mid- and low-frequency bands, with the log-log |Z| slope in the mid-frequency region ranking as the most dominant feature. The dominance of mid- and low-frequency EIS-derived features in the feature importance ranking indicates that impedance variations in this frequency range are more informative for SoH prediction than those at higher frequencies for the data set and model setup used in this work. For the ECM parameters, the feature-importance ranking is strongly dominated by R3, with the constant phase element parameter CPE1_0 emerging as

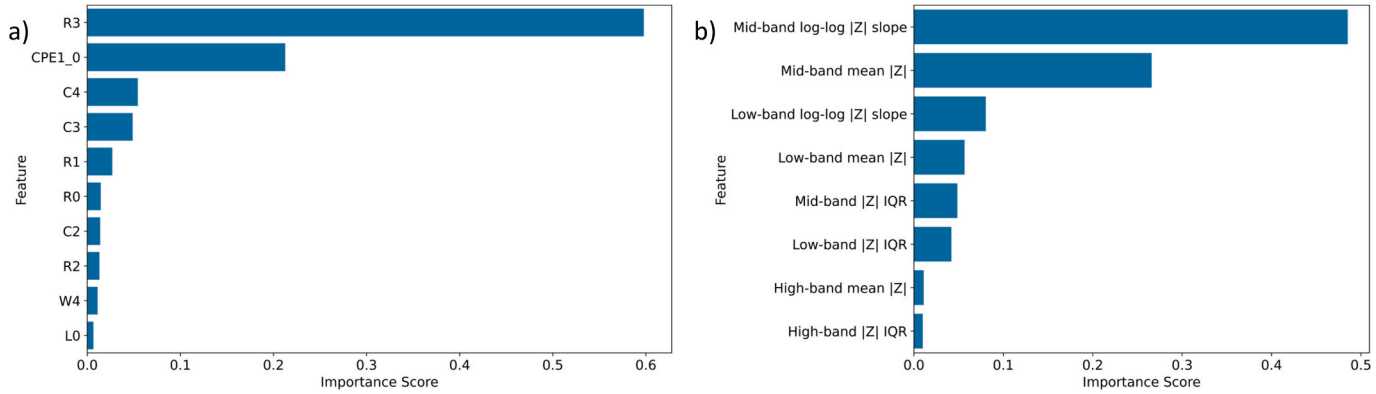


Fig. 3. Feature importance ranking of a) ECM parameters and b) EIS-derived features as determined by the XGBoost base learner used in the ensemble model.

Table 5
Comparison of model performance metrics with ECM parameters and EIS raw dataset.

	Complete feature set		The top four most significant features	
	ECM parameters	*EIS-derived features*	*ECM parameters*	*EIS-derived features*
Validation performance				
Mean absolute error	0.0195	0.0206	0.0217	0.0217
Root-mean-square error	0.0249	0.0266	0.0274	0.0271
R^2	0.8301	0.7455	0.7929	0.7360
Test performance				
Mean absolute error	0.0194	0.0144	0.0231	0.0150
Root-mean-square error	0.0267	0.0194	0.0325	0.0196
R^2	0.7521	0.8567	0.7984	0.8535
FWHM	0.0607	0.0456	0.0622	0.0455

the second most influential feature. The remaining ECM parameters contribute comparatively little to the overall prediction, indicating that the ageing information relevant to SoH estimation is concentrated within a small subset of the fitted circuit parameters. In both representations, the importance scores show a steep decay beyond the top-ranked features, indicating that degradation information is primarily carried by a small number of highly informative descriptors. This observation is consistent with the comparable performance obtained using only the four most significant features, suggesting that the remaining features contribute relatively little additional predictive information. High-frequency features L0 and R0 contribute minimally, suggesting that bulk ohmic behavior alone does not fully account for the observed degradation trends.

3.4. Machine learning model

This subsection presents the performance of the proposed ML model evaluated based on the MAE, RMSE, and R^2 values. Quantitative performance metrics for the models trained using both the full feature sets and the four most significant features are summarized in Table 5. The results show that, although the complete feature set achieves slightly better predictive performance, the reduced feature set still delivers comparable accuracy, with slightly decreased performance metrics. This suggests that only a few features retain most of the predictive information contained in the full feature representations. Fig. 4 visually compares the predicted SoH and its corresponding measured values for the ECM-based and EIS-derived representations. A direct comparison of the two feature representations further highlights the distinction

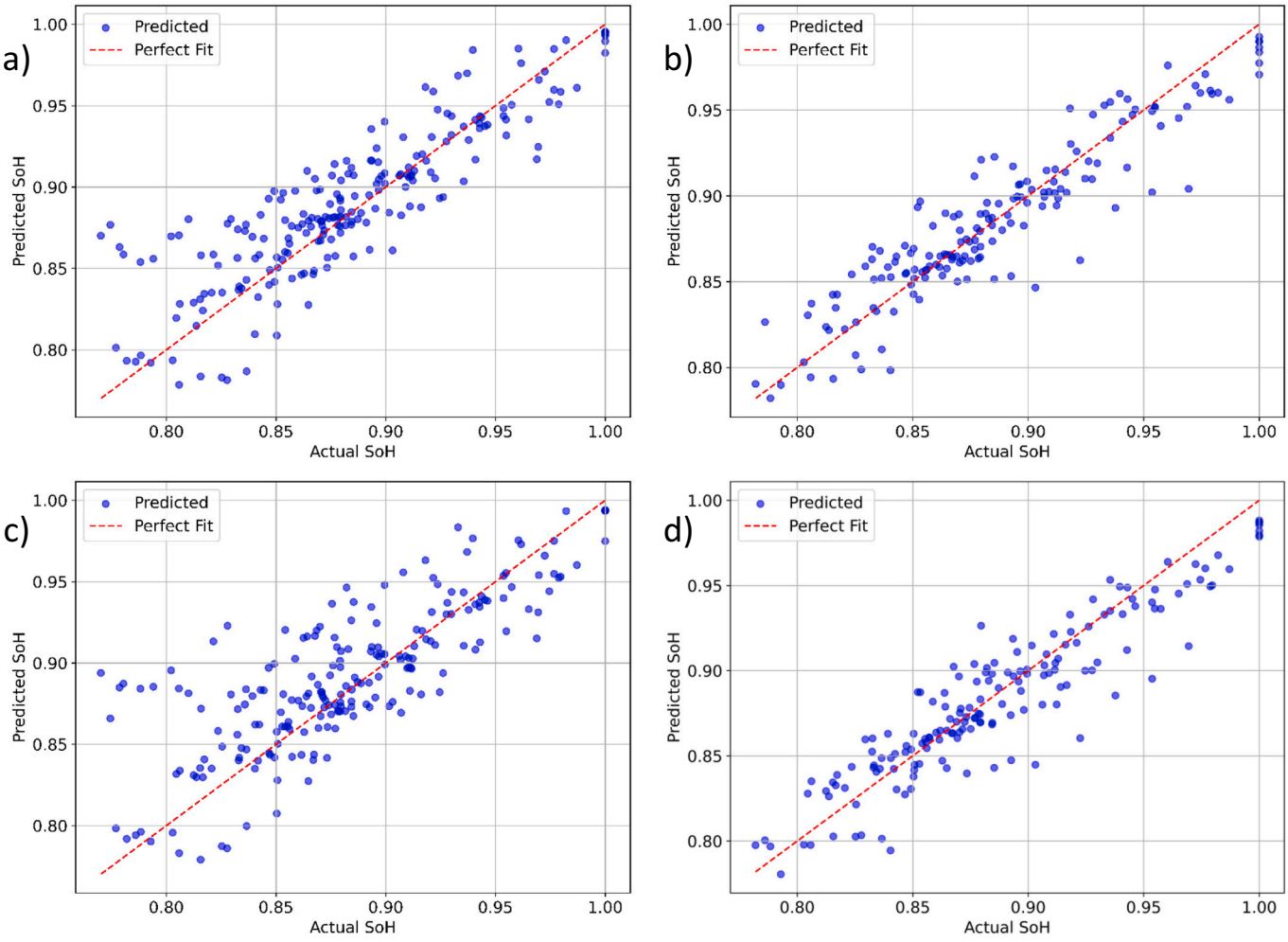


Fig. 4. Scatter plots of predicted versus actual SoH for the stacked ensemble model. (a,b) show results using the full feature sets derived from the ECM parameters and EIS-based representations, respectively, while (c,d) present the corresponding results using only the most significant features from each representation. The red dashed line indicates the line of perfect prediction.

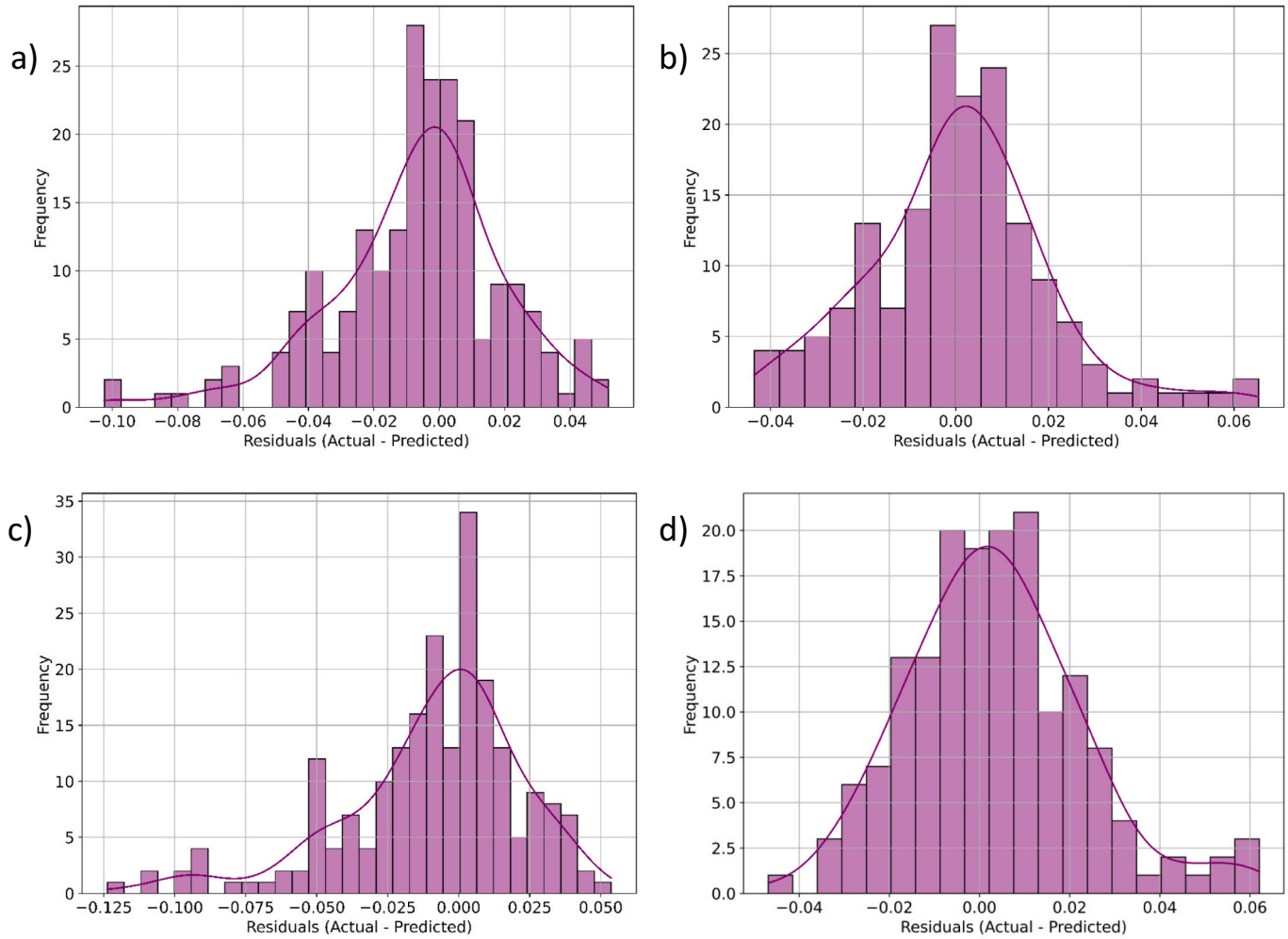


Fig. 5. Histogram plots of the residuals (actual − predicted SoH) for the test data. (a,b) correspond to the full feature sets derived from ECM parameters and EIS-based representations, respectively, while panels (c,d) show the residual distributions obtained using only the top three most significant features from each representation. In all cases, the residuals are approximately normally distributed and centred around zero.

between physically structured ECM parameters and directly extracted EIS-derived spectral descriptors. As shown in Fig. 4(a-d), both representations produce predictions that align closely with the line of perfect agreement, while the EIS-derived features show marginally tighter clustering around the reference line.

The EIS-derived features achieved a slightly higher prediction accuracy than the ECM-based representation. This suggests that the statistical descriptors extracted directly from the impedance spectrum preserve slightly more of the ageing-related information available for SoH estimation. Nevertheless, the performance difference between the two representations remains small, indicating that both compact feature sets effectively capture the degradation information contained within the impedance spectrum. While the EIS-derived features provide a purely data-driven representation, the ECM parameters offer the additional advantage of direct electrochemical interpretability, which may be beneficial for degradation analysis beyond SoH prediction. The residual distributions in Fig. 5a–d correspond to the full and reduced feature sets for both the ECM-based and EIS-derived representations. In all cases, the residual errors are approximately normally distributed and centered around zero, indicating that the dominant ageing trends are well captured and that the remaining deviations arise primarily from stochastic variability rather than systematic bias. The FWHM values were identical for the EIS and ECM representations in both the complete-feature and the reduced-feature representation, indicating comparable error spread and prediction consistency within each setting.

In comparison to similar studies, the SoH predictive performance attained here is comparable to that of other ML methods. GPR-based methods have reported mean absolute errors below 1.5% under controlled conditions [42], while deep learning approaches have been reported to achieve errors of 2% when trained on well-structured datasets and full-cycling data [26]. In this context, the results presented here attained predictive performance comparable to existing ML approaches while being evaluated on a dataset comprising cells aged under fourteen distinct operating conditions. A key advantage of the proposed approach is that this level of performance is obtained using compact feature representations rather than full impedance spectra or highly engineered feature sets. Both the ECM-based and band-compressed EIS-derived representations preserve the electrochemical information most relevant to battery degradation while substantially reducing input dimensionality. Furthermore, the stacking ensemble exploits the complementary learning characteristics of XGBoost and Random Forest to improve prediction robustness, demonstrating that compact, physically meaningful feature representations can provide reliable SoH estimation without relying on high-dimensional impedance data.

4. Conclusion

This study demonstrates the feasibility of combining EIS with ML to estimate the SoH of lithium-ion batteries using data from cells aged

under different conditions. The models were developed and evaluated using EIS measurements acquired from full lithium-ion cells aged under fourteen distinct operating conditions, enabling assessment of the proposed framework across a broad range of degradation trajectories and operating stresses. Model performance was evaluated and compared across two feature representations: band-compressed descriptors derived from the impedance spectra and parameters obtained from ECM fitting. When used within a stacking ensemble comprising XGBoost and Random Forest base learners with a linear regression meta-learner, both feature representations achieved strong predictive performance, with RMSE below 3%, comparable to the accuracy reported in the literature. The feature importance analysis showed that mid- and low-frequency impedance characteristics are the most informative predictors within the EIS-derived feature set. The model also maintained comparable performance when trained on a reduced feature set that includes only the top four most significant features in both feature sets. For the ECM representation, the feature-importance analysis was strongly dominated by the parameter R3, followed by the constant phase element parameter CPE1_0, indicating that most predictive information is concentrated within a small subset of the fitted circuit parameters. Overall, the results show that both physically informed ECM parameters and statistically derived EIS descriptors provide reliable inputs for data-driven SoH estimation. The proposed methodology therefore offers an efficient and interpretable framework for EIS-based battery health estimation while substantially reducing input dimensionality, making it well suited for applications where EIS measurements are available.

CRediT authorship contribution statement

Emmanuel Ezeoba: Writing – review & editing, Writing – original draft, Visualization, Validation, Methodology, Investigation, Formal analysis, Data curation, Conceptualization. **Sehriban Celik:** Writing – review & editing, Conceptualization. **Gereon Stahl:** Writing – review & editing, Validation, Supervision, Resources. **Dirk Uwe Sauer:** Visualization, Supervision, Resources, Funding acquisition.

Declaration of Generative AI and AI-assisted technologies in the writing process

During the preparation of the manuscript, the authors used GPT4/OpenAI and Grammarly to improve readability and language, as they are non-native English speakers. All content was subsequently reviewed and edited by the authors, who take full responsibility for the final publication.

Declaration of competing interest

The authors declare that they have no known competing financial interests or personal relationships that could have appeared to influence the work reported in this paper.

Acknowledgments

The authors gratefully acknowledge the financial support from the German Federal Ministry of Research, Technology and Space, through the DAFODIL project. Funding Code: BMBF 03XP0389E.

Appendix A. Supplementary data

Supplementary data to this article can be found online at https://doi.org/10.1016/j.est.2026.124353.

Data availability

Data will be made available on request.

References

[1] Y. Fan, F. Xiao, C. Li, G. Yang, X. Tang, J. Energy Storage 32 (2020) 101741.
[2] K. Mc Carthy, H. Gullapalli, K.M. Ryan, T. Kennedy, J. Electrochem. Soc. 168 (2021) 080517.
[3] J. Wang, C. Zhang, X. Meng, L. Zhang, X. Li, W. Zhang, Batteries 10 (2024) 139.
[4] L. Fan, P. Wang, Z. Cheng, J. Energy Storage 43 (2021) 103115.
[5] L. Chen, Z. Lü, W. Lin, J. Li, H. Pan, Measurement 116 (2018) 586–595.
[6] W. He, N. Williard, C. Chen, M. Pecht, Int. J. Electr. Power Energy Syst. 62 (2014) 783–791.
[7] P. Vadhva, J. Hu, M.J. Johnson, R. Stocker, M. Braglia, D.J.L. Brett, A.J.E. Rettie, ChemElectroChem 8 (2021) 1930–1947.
[8] Y. Zhang, Q. Tang, Y. Zhang, J. Wang, U. Stimming, A.A. Lee, Nat. Commun. 11 (2020) 1706.
[9] Y. Fu, J. Xu, M. Shi, X. Mei, IEEE Trans. Ind. Electron. 69 (2022) 7019–7028.
[10] J. Lu, R. Xiong, J. Tian, C. Wang, F. Sun, Nat. Commun. 14 (2023) 2760.
[11] A. Barai, K. Uddin, M. Dubarry, L. Somerville, A. McGordon, P. Jennings, I. Bloom, Prog. Energy Combust. Sci. 72 (2019) 1–31.
[12] A.Ch. Lazanas, M.I. Prodromidis, ACS Meas. Sci. Au 3 (2023) 162–193.
[13] N. Meddings, M. Heinrich, F. Overney, J.-S. Lee, V. Ruiz, E. Napolitano, S. Seitz, G. Hinds, R. Raccichini, M. Gaberšček, J. Park, J. Power Sources 480 (2020) 228742.
[14] H. Laufen, S. Berg, J. Engeser, M. Strautmann, A. Koprivc, C. Rahe, E. Figgemeier, D.U. Sauer, Adv. Mater. Technol. 9 (2024) 2301965.
[15] M. Lagnoni, C. Scarpelli, G. Lutzemberger, A. Bertei, J. Energy Storage 94 (2024) 112326.
[16] F. Santoni, A. De Angelis, A. Moschitta, P. Carbone, M. Galeotti, L. Cinà, C. Giammanco, A. Di Carlo, J. Energy Storage 82 (2024) 110389.
[17] Y. Li, M. Maleki, S. Banitaan, J. Energy Storage 73 (2023) 109185.
[18] M. Derakhshan, E. Sahraei, D. Soudbakhsh, Cell Rep. Phys. Sci. 3 (2022) 101102.
[19] X. Shu, S. Shen, J. Shen, Y. Zhang, G. Li, Z. Chen, Y. Liu, iScience 24 (2021) 103265.
[20] Z. Deng, L. Xu, H. Liu, X. Hu, Z. Duan, Y. Xu, Appl. Energy 339 (2023) 120954.
[21] X. Hu, L. Xu, X. Lin, M. Pecht, Joule 4 (2020) 310–346.
[22] S. Guo, L. Ma, Energy 263 (2023) 125872.
[23] G. Bloch, F. Lauer, G. Colin, Y. Chamaillard, Inf. Sci. 178 (2008) 3813–3827.
[24] P. Tsirikoglou, S. Abraham, F. Contino, C. Lacor, G. Ghorbaniasl, Appl. Soft Comput. 61 (2017).
[25] F. Yang, X. Song, D. Wang, K.-L. Tsui, IEEE Access 7 (2019) 88894–88902.
[26] H. Xu, L. Wu, S. Xiong, W. Li, A. Garg, L. Gao, Energy 276 (2023) 127585.
[27] S. Saxena, L. Ward, J. Kubal, W. Lu, S. Babinec, N. Paulson, J. Power Sources 542 (2022) 231736.
[28] A. Jose, S. Shrivastava, Results Eng. 27 (2025) 105825.
[29] Z. Jia, Z. Li, K. Zhao, K. Wang, S. Wang, Z. Liu, J. Energy Storage 97 (2024) 112947.
[30] X. Li, M. Zhao, S. Zhong, J. Li, Z. Cui, S. Fu, Z. Yan, J. Power Sources 650 (2025) 237503.
[31] H. Guo, L. Yu, Y. Ren, A. Sun, J. Yang, J. Energy Storage 130 (2025) 117475.
[32] J. Hu, J. Chang, Z. Zhang, C. Wang, X. Jian, J. Wang, Q. Liu, J. Electrochem. Soc. 173 (2026) 050510.
[33] Q. Xing, M. Zhang, Y. Fu, K. Wang, J. Energy Storage 110 (2025) 115345.
[34] S. Uddin, H. Lu, PLoS One 19 (2024) e0301541.
[35] R.G. Pensa, A. Crombach, S. Peignier, C. Rigotti, Mach. Learn. 114 (2025) 287.
[36] X. Wang, B. Hu, X. Su, L. Xu, D. Zhu, J. Energy Storage 76 (2024) 109796.
[37] S. Jafari, J.-H. Yang, Y.-C. Byun, Results Eng. 24 (2024) 102786.
[38] W. Zhang, R. Ahmed, S. Habibi, J. Power Sources 630 (2025) 236108.
[39] M. Murbach, B. Gerwe, N. Dawson-Elli, L. Tsui, J. Open Source Softw. 5 (2020) 2349.
[40] E. Ezeoba, A. Grade, G. Stahl, D.U. Sauer, J. Energy Storage 179 (2026) 123856.
[41] M. Heinrich, N. Wolff, S. Seitz, U. Krewer, Batteries 8 (2022) 40.
[42] S. Pohlmann, A. Mashayekh, F. Stroebl, D. Karnehm, M. Kuder, A. Neve, T. Weyh, J. Energy Storage 88 (2024) 111649.